Composition, Response to Pressure and Negative Thermal Expansion in $M^{II}B^{IV}F_6$; M – Ca, Mg, B – Zr, Nb

Brett R. Hester,[#] Justin C. Hancock,[#†] Saul H. Lapidus,[‡] and Angus P. Wilkinson*[,#,§]

[#] School of Chemistry and Biochemistry, Georgia Institute of Technology, Atlanta, GA 30332-0400, United States

[‡] X-ray Science Division, Advanced Photon Source, Argonne National Laboratory, Lemont, Illinois 60439, United States

[§] School of Materials Science and Engineering, Georgia Institute of Technology, Atlanta, GA 30332-0245, United States

ABSTRACT: $CaZrF_6$ has recently been shown to combine strong negative thermal expansion (NTE) over a very wide temperature range (at least 10 – 1000 K) with optical transparency from the mid-IR into the UV. Variable-temperature and high-pressure diffraction has been used to determine how the replacement of calcium by magnesium and zirconium by niobium (IV) modifies the phase behavior and physical properties of the compound. Similar to $CaZrF_6$, $CaNbF_6$ retains a cubic ReO_3-type structure down to 10 K and displays NTE up until at least 900 K. It undergoes a reconstructive phase transition on compression to ~400 MPa at room temperature and pressure induced amorphization above ~4 GPa. Prior to the first transition, it displays very strong pressure-induced softening. $MgZrF_6$ adopts a cubic ($Fm\bar{3}m$) structure at 300 K, and undergoes a symmetry lowering phase transition involving octahedral tilts at ~100 K. Immediately above this transition it shows modest NTE. Its' thermal expansion increases on heating, crossing through zero at ~500 K. Unlike $CaZrF_6$ and $CaNbF_6$, it undergoes an octahedral tilting transition on compression (~370 MPa) prior to a reconstructive transition at ~1 GPa. Cubic $MgZrF_6$ displays both pressure-induced softening and stiffening on heating. $MgNbF_6$ is cubic ($Fm\bar{3}m$) at room temperature, but it undergoes a symmetry-lowering octahedral tilting transition at ~280 K. It does not display NTE within the investigated temperature range (100 – 950 K). While the replacement of Zr(IV) by Nb(IV) leads to minor changes in phase behavior and properties, the replacement of the calcium by the smaller and more polarizing magnesium leads to large changes in both phase behavior and thermal expansion.

1. INTRODUCTION

While most materials expand on heating, a growing number are known to contract.[1-4] Such negative thermal expansion (NTE) can, in principle, be used to compensate for the response of positive thermal expansion (PTE) solids, either by preparing composites of the PTE and NTE materials or by assembling devices containing parts made from separate NTE and PTE components. There is a significant body of work examining the fabrication and performance of metal matrix-ceramic composites, polymer ceramic composites, and ceramic-ceramic composites containing NTE materials for various applications.[5-10] When NTE and PTE solids are used together in a composite, there can be considerable stresses within the composite due to differential thermal expansion. These stresses can lead to phase transitions and other unwanted phenomena,[11-12] as open framework NTE solids typically display quite rich behavior at low pressure.[13-18]

The mechanisms and compositions associated with NTE materials are varied. In open framework oxides, fluorides, cyanides, and MOFs, low frequency phonons can give rise to NTE and other unusual phenomena, such as pressure induced softening.[13] NTE can also be associated with structural phase transitions,[19] charge transfer,[20] ferroelectric instabilities,[21-22] and magnetic ordering effects.[23] It has also been reported in 2D materials such as graphene.[24]

While much of the earlier work on NTE solids focused on oxides, metal fluorides with ReO_3-type structures have recently attracted attention.[18, 25-33] Materials such as ScF_3[28] and $CaZrF_6$[18] combine strong or very strong isotropic negative thermal expansion with optical transparency ranging from the mid-IR into the UV, suggesting optical applications. For some applications, less extreme NTE is desirable. There has been some success in tuning the characteristics of ScF_3 by solid solution formation[25-27, 30, 34] and nanosizing,[35] and very recently a suite of $MZrF_6$ compositions (M – Ca, Mn, Fe, Co, Ni and Zn)[33] have been examined in or-

der to better understand the extent to which the very strong NTE found in $CaZrF_6$, and its close relative $CaHfF_6$, can be tailored. The remarkable NTE of both ScF_3 and $CaZrF_6$ is associated with the stability of the ideal cubic ReO_3 structure towards symmetry lowering phase transitions when cooled to very low temperatures. This has been attributed to the high ionicity of these compounds.[18, 28] To the extent that information is available, MF_3 and $M^{II}B^{IV}F_6$ with ReO_3-type connectivity and symmetries lower than that of the ideal cubic structure ($Pm\bar{3}m$ and $Fm\bar{3}m$) at close to room temperature do not show strong NTE.

The literature on ReO_3-type $M^{II}B^{IV}F_6$ indicates that mid and late 3d metals on the M –site, such as Fe, Co, Ni and Zn destabilize the cubic structure and, hence, are likely to preclude strong NTE.[36-37] Phase transition temperatures have been reported to range from ~400 K for Ni to ~150 K for Mn in $MZrF_6$,[36] although contrary to this, and other literature on $CoZrF_6$,[18, 38] a very recent paper on thermal expansion in $MZrF_6$ reports no phase transitions for the Co and Ni materials above 125 K.[33] In this paper, we examine how the replacement of Ca^{2+} and Zr^{4+} by Mg^{2+} and Nb^{4+}, effects the thermal expansion and behavior under pressure of ReO_3-type $M^{II}B^{IV}F_6$. Variable-temperature neutron and/or synchrotron x-ray diffraction were employed to study the phase behavior and thermal expansion of $MgZrF_6$, $CaNbF_6$, and $MgNbF_6$, and high-pressure synchrotron x-ray powder diffraction was used to examine the behavior of $MgZrF_6$ and $CaNbF_6$.

2. EXPERIMENTAL

2.1. Syntheses.

All syntheses were carried out in a dry, nitrogen-filled glove-box. NbF_5 (99.5%) was purchased from STREM Chemicals, ZrF_4 (99.9%) from Sigma Aldrich, and niobium metal powder (99.99% with < 500 ppm Ta), CaF_2 (99.5%) and MgF_2 (99.9% optical grade) from Alfa Aesar. As several different batches of material were used for the reported measurements on $CaNbF_6$ and $MgZrF_6$, we report representative syntheses for these materials.

NbF_4 was prepared via the solid state reaction of NbF_5 and niobium metal using a procedure similar to that reported by Chassaing et al.[39] The reactants were mixed in a 5:1 molar ratio and then placed into a copper tube, which was sealed by arc-welding under argon. The copper tube was then sealed in an evacuated fused quartz ampule. The ampule was heated to 300 °C (heating rate: 0.19 °C/min), held at 300 °C for 96 hrs, and then quenched. The excess NbF_5 was removed from the resulting mixture by vacuum sublimation. The resulting NbF_4 was a black hygroscopic powder. Note that NbF_4 is reported to disproportionate at greater than 350 °C.[40]

$CaNbF_6$ and $MgNbF_6$ were prepared via the solid state reaction of NbF_4 and MF_2 (M= Ca, Mg), using a procedure based on that reported by Goubard et al.[41] The reactants were mixed in a 1:1 molar ratio and placed into a copper tube, which was then sealed via arc-welding under argon. The copper tube was then sealed in an evacuated fused quartz ampule. The ampule was heated to 520 °C (heating rate: 4.13 °/min), held at 520 °C for 5 days, and slowly cooled to room temperature. The final $CaNbF_6$ and $MgNbF_6$ products were grey and black powders respectively.

$MgZrF_6$ was prepared via the solid state reaction of ZrF_4 and MgF_2. The reactants were mixed in a 1:1 molar ratio and placed into a copper tube, which was then sealed via arc-welding under an argon atmosphere. The copper tube was then sealed in an evacuated fused quartz ampule. The ampule was heated to 850 °C (heating rate: 4.13 °/min), held at 850 °C for 24 hrs, and then slowly cooled to room temperature. The final $MgZrF_6$ product was a white powder.

Sample syntheses for the x-ray measurements were performed typically on a ~500 mg scale. However, sample preparation for the $CaNbF_6$ neutron measurements was performed on a ~4 g scale.

The starting materials NbF_5 and ZrF_4 are moisture sensitive and the products $CaNbF_6$, $MgNbF_6$ and $MgZrF_6$ are expected to show some sensitivity to atmospheric exposure. After storage for several months, $CaNbF_6$ samples showed signs of decomposition, but exposure to the laboratory atmosphere for several hours led to little change in the powder x-ray diffraction patterns for $MgNbF_6$ and $MgZrF_6$.

2.2. Variable temperature X-ray powder diffraction measurements

X-ray powder diffraction data were recorded using an Oxford Cryosystems Cryostream (100 – 500 K), for samples of $CaNbF_6$, $MgZrF_6$ and $MgNbF_6$. Data were also recorded using a resistively heated furnace (300 – ~1000 K). These measurements were performed at the 17-BM beamline of the Advanced Photon Source, Argonne National Laboratory, using precisely determined wavelengths close to 0.73 Å. The low temperature measurements were performed using samples that were sealed using epoxy in Kapton capillary tubes under an inert gas atmosphere. For the furnace measurements, the samples were contained in fused quartz capillaries with helium gas flowing very slowly though them.

Additionally, low temperature high resolution synchrotron powder diffraction data were recorded for a sample of $MgZrF_6$ at beam line 11-BM of the Advanced Photon Source,[42-43] using an Oxford Instruments closed-flow helium cryostat (OptistatCF). An average wavelength of 0.41421 Å was used for these measurements.

For each of the above measurements, < 100 mg of material was needed as small diameter (~1 mm or less) capillaries were used.

2.3. Neutron powder diffraction measurements

Neutron diffraction measurements were made using the PAC (POWGEN Auto-Changer) sample environment on the POWGEN beam line at the Spallation Neutron Source, Oak Ridge National Laboratory. A $CaNbF_6$ sample was loaded into a vanadium can under helium. The sample was cooled to 10 K and heated in steps to 300 K with 3 minute equilibration times at each temperature prior to recording a diffraction pattern.

2.4. High pressure X-ray diffraction measurements

High pressure X-ray powder diffraction data (298 K and P < ~8.6 GPa) were recorded for samples of $CaNbF_6$ and $MgZrF_6$ at beam line 17-BM of the Advanced Photon Source using an EasyLab "Diacell Bragg-(G)" diaphragm diamond anvil cell (DAC) while the pressure was continuously increased. The sample was loaded under inert atmosphere with either NaCl or CaF_2 as an internal pressure calibrant and an Alfa silicone oil (molecular weight of 237 $g \cdot mol^{-1}$) as the pressure-transmitting fluid. Pressure was determined using the unit cell volumes of the NaCl or CaF_2, along with their known equations of state (Birch EoS for NaCl[44] and the EoS reported by Angel et al.[45] for CaF_2).

High-pressure X-ray diffraction data (P < 310 MPa, 298 K < T < 523 K) were also recorded for $MgZrF_6$ at the 11-ID-B beam-line of the Advanced Photon Source using a heated titanium pressure vessel and Background Reducing Internal Mask (BRIM)[46] as previously described.[27] This arrangement allows for precise control of both temperature and pressure.

2.5. Rietveld analyses of the powder diffraction data

Rietveld refinements were used to determine structural parameters and lattice constants. All the fits were done using the General Structure Analysis System (GSAS)[47] along with the EXPGUI[48] interface.

3. RESULTS AND DISCUSSION

3.1. Phase behavior and expansion as a function of temperature

All the materials under study were examined using variable temperature synchrotron powder diffraction over the temperature interval 100 – 500 K. Additionally, $CaNbF_6$ was examined by powder neutron diffraction between 10 and 300 K and $MgZrF_6$ was studied by high resolution synchrotron x-ray diffraction at down to 10 K. High temperature synchrotron powder diffraction experiments were performed for all the materials, but in some cases the data are only qualitatively useful due to difficulties with temperature control.

3.1.1. Behavior of $CaNbF_6$ from 10 to 900 K

Powder x-ray and neutron diffraction show that $CaNbF_6$ remains cubic and displays negative thermal expansion over the entire temperature range studied. The 10 K neutron powder diffraction pattern is fully consistent with rock salt like cation ordering in a cubic ReO_3-type structure with $Fm\bar{3}m$ symmetry (Fig. 1)

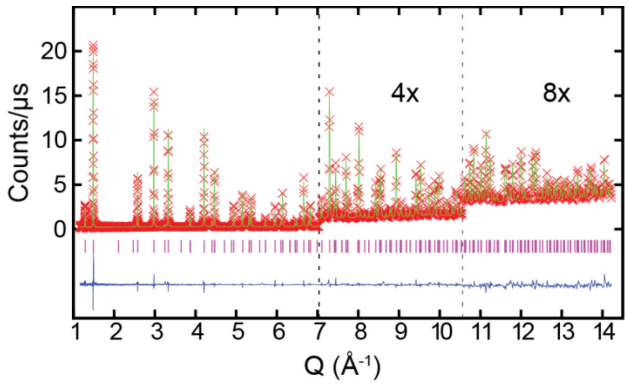

Figure 1. Rietveld fit to a 10 K time-of-flight powder neutron diffraction pattern for $CaNbF_6$ using a cation ordered cubic ReO_3-type model.

The lattice constants and derived thermal expansion coefficients from the neutron diffraction data (Fig. 2) show strong NTE, very similar to that previously seen for $CaZrF_6$, but with greater magnitude; α_v ~ -65 x10^{-6} K^{-1} at ~70 K for $CaNbF_6$ compared to α_v ~ -56 x10^{-6} K^{-1} at ~ 75 K for $CaZrF_6$.

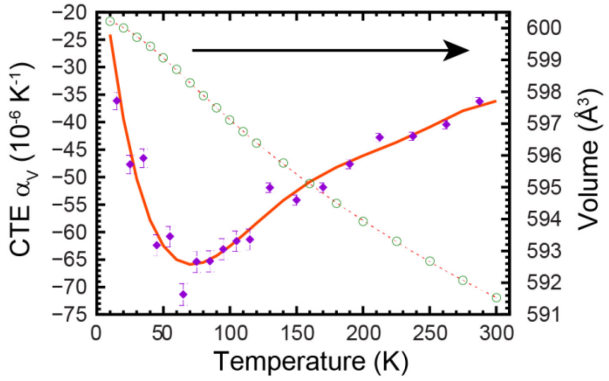

Figure 2. Unit cell volume and volume thermal expansion coefficient for $CaNbF_6$ determined from the powder neutron diffraction data. A six term polynomial fit to the volume (dashed line) was used to calculate the expansion coefficient (solid orange line). Additionally, the expansion coefficient was determined point by point (purple symbols).

The magnitude of the NTE generally decreases on heating (Fig. S1), but it persists to above the temperature used to synthesize the material (~800 K), even after the sample begins to decompose. The high temperature diffraction data for $CaNbF_6$ (Fig. S2) suggest that the initial decomposition products are CaF_2 and a ReO_3-type phase, which may be a niobium oxyfluoride. As NbF_4 is known to disproportionate at high temperatures,[39-40] and NbF_5 reacts with SiO_2,[49] the oxyfluoride could arise from reaction with the fused quartz capillary tube used to contain the sample.

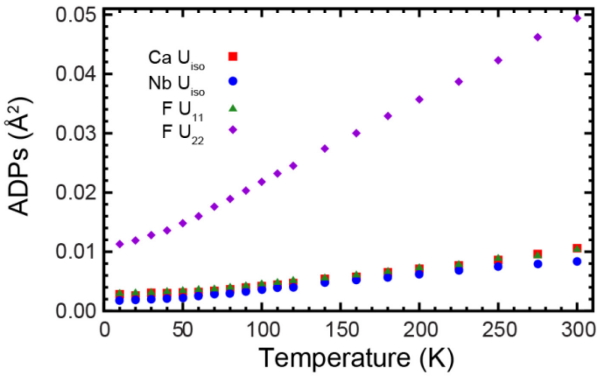

Figure 3. Atomic displacement parameters for $CaNbF_6$ determined from the Rietveld analyses of the neutron diffraction data.

The atomic displacement parameters (ADPs) obtained by Rietveld analysis of the neutron diffraction data (Fig. 3) are consistent with the expected rigid unit mode (RUM) like mechanism for NTE in this material. The transverse component of the ADP for the fluoride is much bigger than the longitudinal one and it increases rapidly with temperature. The large value for U_{22}(F) at very low temperatures, similar to that found in $CaZrF_6$, is indicative of large amplitude zero point motion associated with a wide-bottomed potential for distortions involving the displacement of fluoride in this direction.

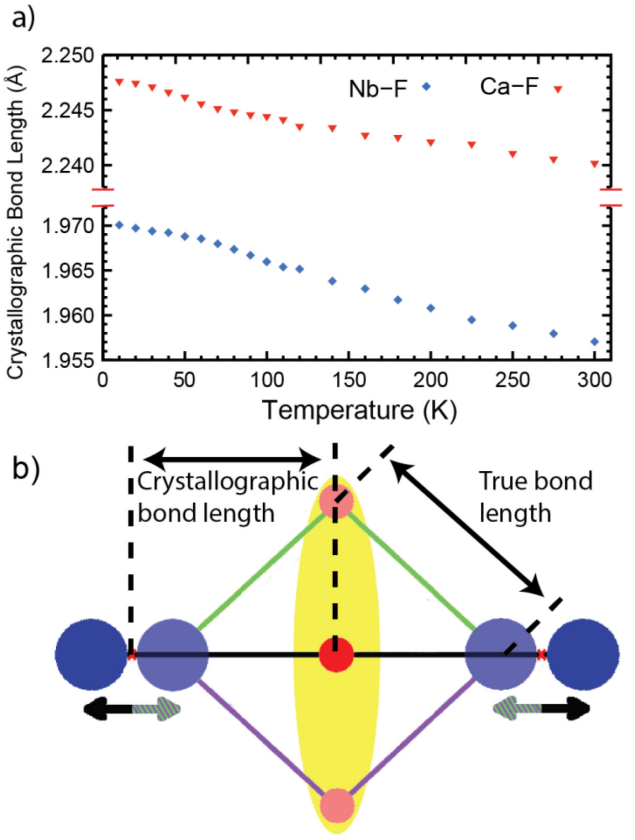

Figure 4. a) Apparent (crystallographic) Ca-F and Nb-F bond lengths, obtained from Rietveld analyses of the neutron diffraction data for $CaNbF_6$, as a function of temperature. b) Schematic showing how the transverse vibrational motion of fluoride (red/pink) couples to the motion the metals (blue) leading to an apparent decrease in crystallographic bond length when there is little, or no, increase in the true M-F distances.

Both the crystallographic (apparent) Ca-F and Nb-F bond lengths decrease as the sample is heated from 10 to 300 K (Fig. 4a). These decreases, which are not constant with temperature or equal for the two different crystallographic bond lengths, arise from the combination of an increase in the true bond lengths and an increase in the average displacement of the fluorine perpendicular to the Ca-Nb direction as the material is heated. The later contributes to a decrease in the crystallographic (apparent) bond lengths, as crystallography determines the distances between the average atomic positions, and the former partially counteracts this (Fig. 4b). The inequivalent behavior of the Ca-F and Nb-F distances suggests a greater increase in the true Ca-F distance than the true Nb-F distance as the material is heated.

3.1.2. Behavior of $MgNbF_6$ from 100 to 900 K

Powder X-ray diffraction data for $MgNbF_6$ clearly show a structural phase transition from cubic ($Fm\bar{3}m$) to lower symmetry on cooling below ~280 K (Fig. 5a). The diffraction data show evidence for phase coexistence over a narrow temperature range, suggesting that the transition is first order. The data for the low temperature phase could be fit using a cation ordered ReO_3-type model with $R\bar{3}$ symmetry similar to that previously reported for $CoZrF_6$,[38] although there was clear evidence of some scattering between the newly split Bragg peaks (Fig. 5b). Scattering of this type is quite often seen below ferroelastic phase transitions and can be attributed to strains associated with domain boundaries in the twinned low temperature material.[50]

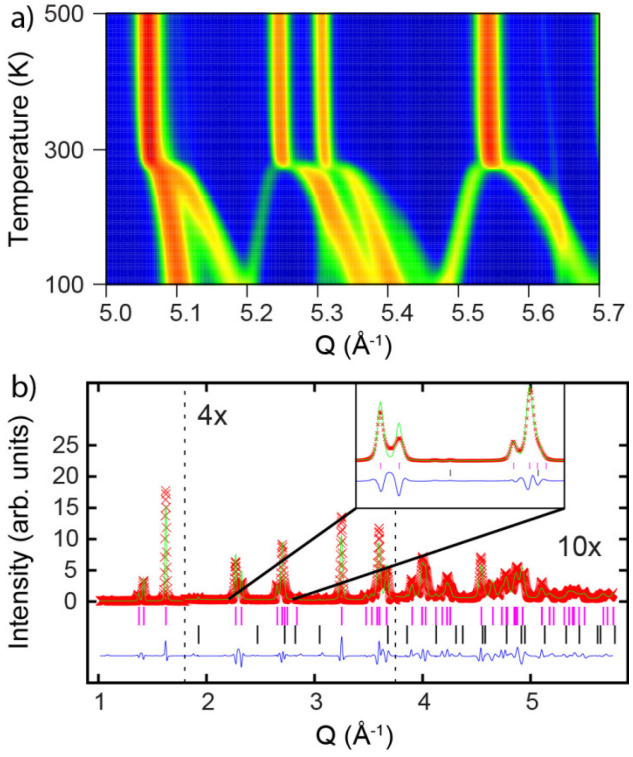

Figure 5. a) Synchrotron x-ray data for $MgNbF_6$ showing an apparently discontinuous phase transition at ~281 K. The individual diffraction patterns were recorded at 3 K intervals after equilibrating the sample. b) Data (100 K) for the low symmetry phase could be fit with a $R\bar{3}$ model. The fit quality suggests a significant contribution to the scattering from strained material in domain walls, which is not accounted for by the crystallographic model. The second phase (black tag marks) is unreacted MgF_2 (~2 weight %).

The phase transition is associated with a large increase in unit cell volume per formula unit (Fig. 6a) on heating and a decrease in the magnitude of the volume CTE (Fig. 6b) after the transition. However, the CTE remains positive, even in the cubic phase, until the decomposition of the sample ~950 K (Fig. S3), which probably arose from failure of the fused quartz sample tube during the measurement.

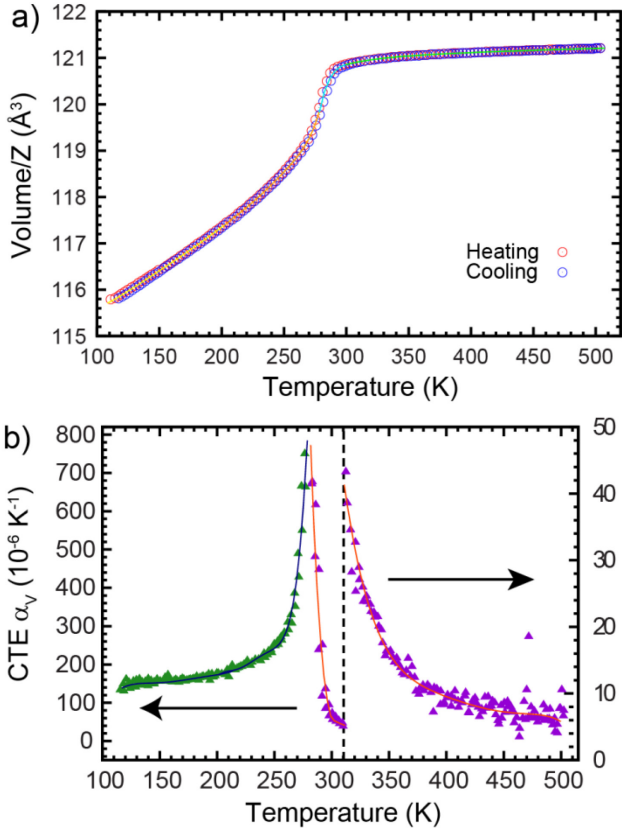

Figure 6. a) The volume per formula unit and b) volume thermal expansion coefficient for $MgNbF_6$ determined from powder x-ray diffraction data. The values were obtained from single phase Rietveld fits with a change from cubic to rhombohedral models at ~280 K.

The thermal expansion of $MgNbF_6$ in the $R\bar{3}$ phase is highly anisotropic (Fig. S4). The material displays very strong positive thermal expansion in the a – b plain ($\alpha_{a(200\text{-}250\ K)}$ ~120 x10^{-6} K^{-1}), which lies perpendicular to the 3-fold axis that the MF_6 octahedra are rotating around, and more modest negative thermal expansion parallel to the 3-fold axis ($\alpha_{c(200\text{-}250\ K)}$ ~-38 x10^{-6} K^{-1}).

3.1.3. Behavior of $MgZrF_6$ from 10 to 900 K

The response of $MgZrF_6$ to changes in temperature was examined by low temperature high resolution synchrotron powder diffraction (10 – 150 K and 300 K), and synchrotron powder diffraction over the range 100 – 500 K and 300 – 900 K. The low temperature experiments showed clear evidence of a symmetry lowering phase transition in the vicinity of 100 K (Figure 7). Unlike the case of $MgNbF_6$ shown in Fig. 5, these data suggest a continuous, or almost continuous, phase transition. However, the precise transition temperature appeared to vary between experiments. While this may have a contribution from differences in thermometry between the measurements, it could also have a contribution from variations in stoichiometry between the different samples. $MgZrF_6$ can readily accommodate excess zirconium fluoride,[51] to form materials of the type $Mg_{1-x}Zr_{1+x}F_{6+2x}$, and although our syntheses targeted perfect stoichiomety, some unreacted MgF_2 (~3.5 wt % in the sample used for the high resolution measurements) are apparent in the diffraction data.

Rietveld analyses of the high resolution x-ray data and the neutron data for the low temperature phase using an $R\bar{3}$ model produced less than ideal fit quality. Notably, scattering is seen between the Bragg peaks expected for this symmetry, which is probably related to the presence of strains at domain boundaries, as was suggested for $MgNbF_6$.

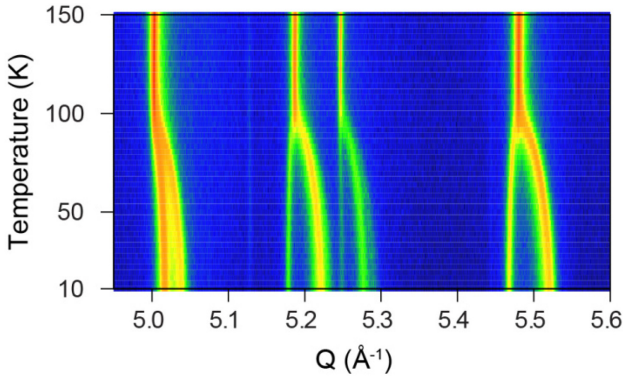

Figure 7. High resolution synchrotron powder x-ray diffraction data for $MgZrF_6$ showing a symmetry lowering phase transition at ~100 K, which appears to be continuous unlike that seen for $MgNbF_6$ (see Fig. 5a).

Above the phase transition the data was fit with a cation ordered cubic ReO_3-type model ($Fm\bar{3}m$) (Fig. S5). The thermal expansion varied from modestly negative just above the transition, with a minimum α_V of ~-12 x10^{-6} K^{-1} at ~170 K, to modestly positive at high temperature, ~+15 x10^{-6} K^{-1} at ~1000 K, crossing through zero at ~ 500 K (Fig. 8). Below the phase transition at ~100 K fits using a $R\bar{3}$ model were performed. The quality of these fits was less than ideal, presumably due to stresses as domain boundaries (Fig. S6). The low temperature phase displays strongly positive volume thermal expansion (Fig. 8a), but the expansion is highly anisotropic with NTE ($\alpha_{c(30\text{-}80\ K)}$ ~-14 x10^{-6} K^{-1}), parallel to the 3-fold axis in the $R\bar{3}$ model

and very strong positive thermal expansion ($\alpha_{a(30\text{-}80\ K)}$ ~70 x10^{-6} K^{-1}) in the a-b plain (Fig. S7).

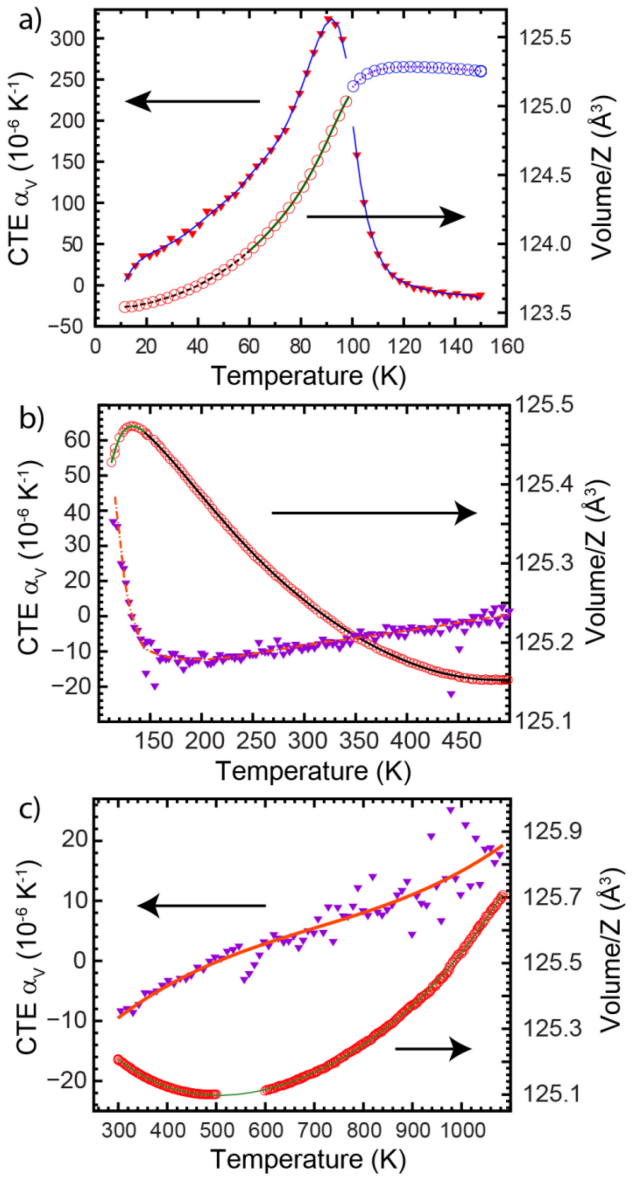

Figure 8. Volume per formula unit versus temperature and coefficient of thermal expansion for $MgZrF_6$ measured by synchrotron powder diffraction using a) a helium cryostat, b) a cryostream cooler and c) a wire wound furnace. The volumes were fit to a polynomial (solid line through the data) which was differentiated to estimate the CTE. The purple/red points are CTE estimates obtained by taking the difference between unit cell volumes. In a) separate polynomials were fit to the low temperature ($R\bar{3}$) and high temperature ($Fm\bar{3}m$) phases. The volumes shown in these panels have not been scaled to take into account calibration differences between the different experimental arrangements

3.2. Phase behavior and compressibility as a function of pressure

The behavior of $CaNbF_6$ on compression was examined using a DAC at pressures up to 8 GPa using a low molecular weight silicone oil as the pressure medium. $MgZrF_6$ was examined in the same way, however, additional measurements were performed for $MgZrF_6$ at pressures up to 300 MPa in the temperature range 300 – 525 K, using an oil-filled pressure cell.[46]

3.2.1. Behavior of $MgZrF_6$ on compression

Diffraction data for $MgZrF_6$ as it is compressed in a DAC are shown in Figure 9a. These data indicate that at least two phase transitions occur below 8 GPa, with transitions at ~0.37 and 1.0 GPa.

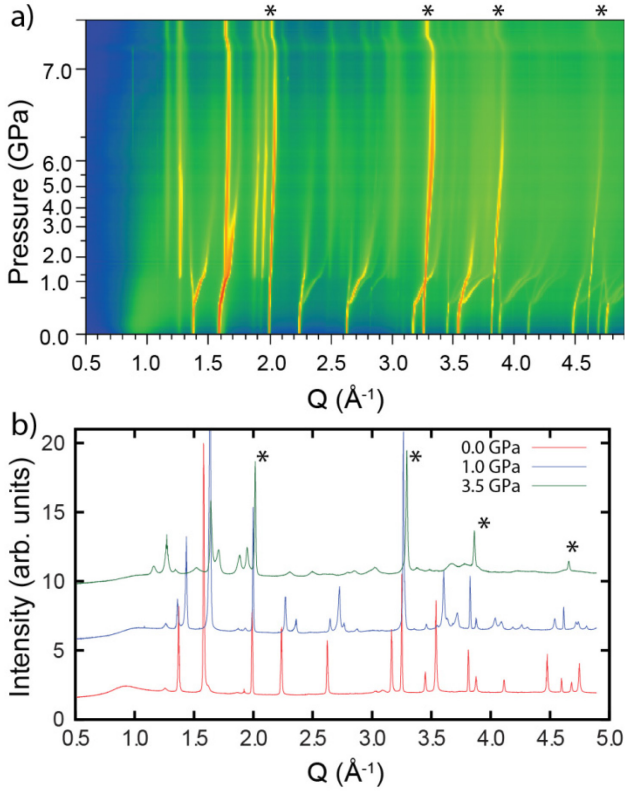

Figure 9. Diffraction data for $MgZrF_6$ on compression in a DAC (* indicate peaks from the CaF2 pressure marker). a) 2D contour plot providing an overview of the phase behavior and b) a comparison of the ambient, 1.0 and 3.5 GPa data.

The initial cubic ($Fm\bar{3}m$) phase persists until ~370 MPa. At this pressure, peak splitting consistent with a phase transition involving octahedral tilts while maintaining the connectivity and cation ordering of the original ReO_3-type structure is observed. The data for this phase are broadly consistent with $R\bar{3}$ symmetry. At ~ 1.0 GPa, the patterns change quite abruptly, consistent with a reconstructive phase transition. The data show evidence for this new phase up until the highest pressures explored and on decompression of the DAC. However, the diffraction patterns for this new phase (Fig. 9b), which show considerable broadening and peak overlap, could not be indexed. Interestingly, the strongest peaks from the new phase can be seen in the starting sample suggesting that the process of finely grinding the $MgZrF_6$ prior to loading it into the DAC irreversibly transformed some of the initial cubic material to this high-pressure phase.

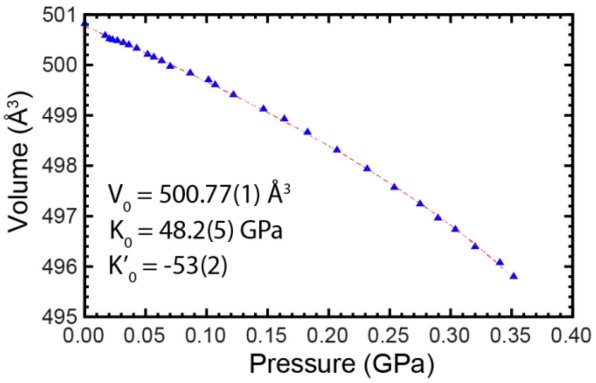

Figure 10. Volume versus pressure, determined from the Rietveld analysis of the DAC data for the ambient pressure form of $MgZrF_6$, along with a fit to a 3rd order Birch-Murnaghan equation of state (EoS). The best fit parameters for the EoS are given in the inset.

The variation of unit cell volume with pressure for cubic $MgZrF_6$ is shown in Fig. 10, along with a best fit to a Birch-Murnaghan (BM) 3rd order equation of state (EoS), performed using EosFit7.[52-53] This phase, with K_0 48.2(5) GPa, is stiffer than $CaZrF_6$ ($K_{0(298\ K)}$ ~ 36 GPa)[18] but softer than ScF_3 ($K_{0(298\ K)}$ ~ 60 GPa).[27] Remarkably, it shows a dramatic softening on compression prior to the phase transition at ~ 350 MPa, with K_0', the pressure derivative of the bulk modulus, ~ -53(2). Pressure induced softening has been observed in other NTE materials, such as $Zn(CN)_2$,[54-55] and predicted by Dove and coworkers to be a general characteristic of frameworks solids that display NTE.[56-58] However, softening on compression is also well known to be a precursor of structural phase transitions.

The behavior of cubic ReO_3-type $MgZrF_6$ was further investigated as a function of temperature and pressure using a heated oil-filled pressure cell that allows for the precise control of both temperature and pressure. A representative Rietveld fit and the lattice constants obtained from these data are available in the supplementary material (Fig. S8 and Table S5). These lattice constants were analyzed using several different approaches. Bulk moduli as a function of temperature, derived from the lattice constants using straight lines fits of ln(V) versus P and the fit of a 2nd order BM EoS, are shown in Fig. 11.

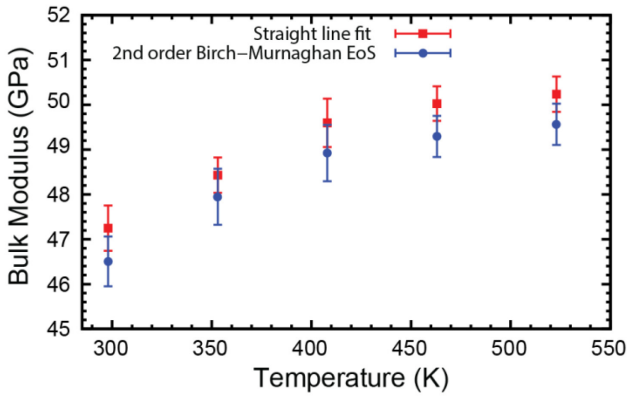

Figure 11. Bulk moduli as a function of temperature for cubic $MgZrF_6$, obtained by fitting a straight line to Ln(V) versus P, and also a 2nd order Birch-Murnaghan equation of state.

Both of these analyses give room temperature zero pressure bulk moduli slightly lower than those obtained when using a 3rd order BM EoS to analyze the data acquired using a DAC (Fig. 10) and indicate that the phase stiffens on heating, which is contrary to the behavior of most materials and that previously observed for $CaZrF_6$. We attribute the slight discrepancy between zero pressure bulk moduli to the different assumptions used for the pressure derivative of the bulk modulus. In a simultaneous analysis of all the PVT data, obtained with a BRIM and heated pressure cell for cubic $MgZrF_6$, using a 3rd order BM EoS and the Berman model for temperature dependent thermal expansion in EOSFit7, the following parameters were obtained: $K_{0(298\ K)}$ = 50.4(7) GPa, K'_{298K} = -16(3), dK_0/dT = 0.015(2) $GPaK^{-1}$, α_0 = -0.81(3) x 10^{-5} and α_1 = 3.4(3).

3.2.2. Behavior of $CaNbF_6$ on compression

Two independent DAC diffraction experiments, with different sample to detector distances, were performed. As the behavior seen in these experiments was the same, only the results from one are presented. Diffraction data for $CaNbF_6$ as it is compressed in a DAC are shown in Fig. 12a. They indicate the onset of a reconstructive phase transition at ~ 400 MPa and a quite abrupt amorphization at ~ 4 GPa. This behavior contrasts with that seen for $MgZrF_6$, where the material was unstable with respect to an octahedral phase transition on compression, but is similar to that previously reported for $CaZrF_6$. The diffraction data in Fig. 12a and 12b suggest that the initial sample contained traces of the high-pressure phase, presumably from grinding the sample prior to loading the DAC. A 3rd order BM EoS was used to fit the V versus P values obtained by Rietveld analysis of the data for cubic ReO_3-type $CaNbF_6$. With $K_{0(298K)}$ = 33.7(4) GPa, $CaNbF_6$ is softer than $MgZrF_6$ ($K_{0(298K)}$ = 48.2(5) GPa) and comparable to, although apparently slightly softer than $CaZrF_6$ ($K_{0(298K)}$ ~36 GPa). $CaNbF_6$ displays quite large pressure induced softening, with $K'_{0(298\ K)}$ ~ -23(2).

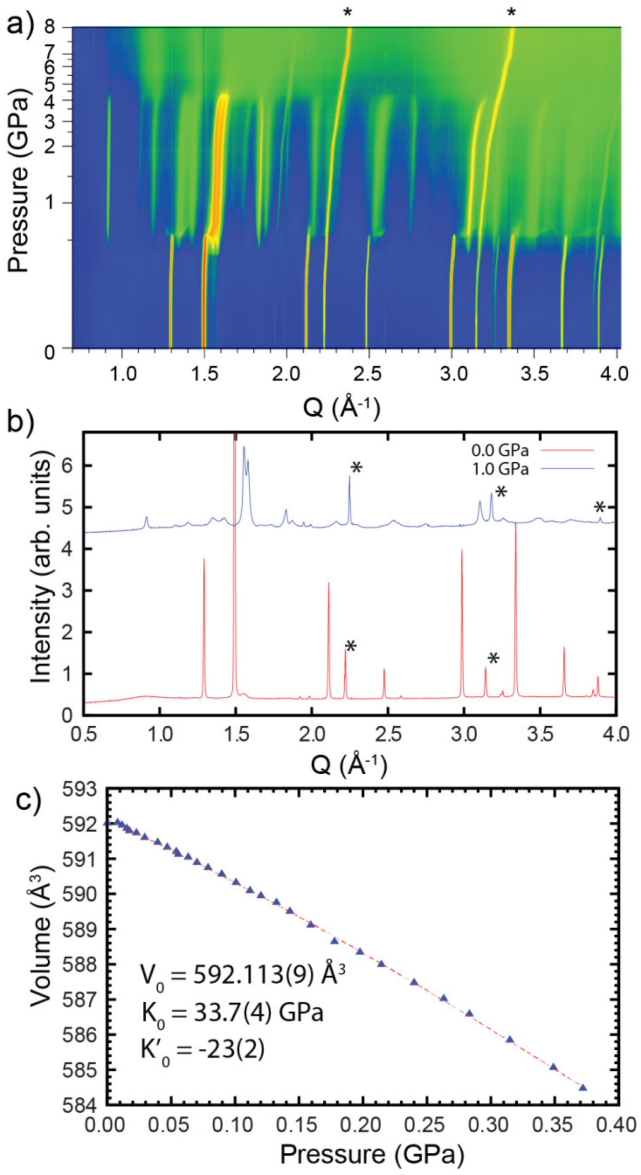

Figure 12. a) Diffraction data as a function of pressure for $CaNbF_6$ on compression in a DAC (* indicate peaks from the NaCl pressure marker). b) Selected diffraction patterns. c) Volume versus pressure for the ambient pressure phase along with a fit to a 3rd order Birch-Murnaghan equation of state.

4. CONCLUSIONS

The replacement of calcium in $CaZrF_6$ by magnesium has a far greater effect on the phase behavior, thermal expansion and elastic properties of ABF_6 than the substitution of zirconium by niobium (IV). Similar to $CaZrF_6$,[18] $CaNbF_6$ retains a cubic cation ordered ReO_3-type structure on cooling to at least 10 K. This phase displays very strong volume NTE with a maximum value of ~-65 x10^{-6} K^{-1} at 70 K, which is slightly larger in magnitude than that previously reported for $CaZrF_6$. High pressure diffraction studies on $CaNbF_6$ indicate that on volume reduction a phase transition involving reconstruction of the framework becomes favorable (~400 MPa) before any of the vibration modes involving octahedral tilts fully soften and give rise to a lower symmetry ReO_3-type framework. Similar behavior was also reported for $CaZrF_6$,[18] but the details of the transition and the stability of the new phase upon further compression appear to be different. ReO_3-type $CaNbF_6$ is slightly softer than $CaZrF_6$ (K_0 ~34 versus ~36 GPa) and displays quite pronounced pressure induced softening on compression. Such pressure induced softening has been reported for other families of NTE solids[54-55] and has been predicted to be common among NTE materials.[56-58] Replacement of calcium by magnesium leads to major changes in phase behavior. On cooling, ReO_3-type $MgZrF_6$ undergoes a symmetry lowering phase transition at around 100 K. The transition appears to be either continuous or almost continuous. At temperatures immediately above the transition, $MgZrF_6$ displays modest NTE (greatest magnitude at ~175 K, α_v ~ -15 x10^{-6} K^{-1}). On warming the thermal expansion becomes positive, crossing through zero at close to 500 K. Diffraction data for the low temperature phase are broadly consistent with an $R\bar{3}$ structure, as previously reported for the low temperature form of $CoZrF_6$.[18, 38] However, the Rietveld fits were less than optimal presumably due to the existence of strains in regions close to the domain boundaries below the ferroelastic transition. On compression at room temperature cubic $MgZrF_6$, unlike cubic $CaNbF_6$, undergoes a phase transition that is associated with octahedral tilts (370 MPa) prior to undergoing a reconstructive phase transition at ~1 GPa. This behavior is consistent with the transition seen on cooling the material. Cubic $MgZrF_6$ is considerably stiffer than $CaNbF_6$ (K_0 ~48 versus ~34 GPa) and shows a greater pressure induced softening at room temperature [K'_0 -53(2) versus -23(2)]. The replacement of both calcium and zirconium to give $MgNbF_6$ leads to even greater destabilization of the cubic ReO_3-structure than the replacement of calcium alone. Cubic $MgNbF_6$ undergoes a symmetry lowering phase transition, to a material that probably has an $R\bar{3}$ structure, at just below room temperature (~280 K). The cubic phase does not show negative thermal expansion in the temperature range that was examined unlike $CoZrF_6$, which has a similar cubic to $R\bar{3}$ phase transition temperature (~270 K),[18] and displays modest NTE above the transition.

Metal fluorides such as $CaZrF_6$, $CaNbF_6$ and $MgZrF_6$ typically have good transparency into the infra-red, as was previously shown for $CaZrF_6$.[18] $CaZrF_6$ also has no transitions in the visible region due to the d^0 electron configurations of both Ca^{2+} and Zr^{4+} and the large electronegativity difference between fluorine and these metals. The replacement of zirconium in $CaZrF_6$ by niobium (IV) leads to absorptions in the visible region due to the d^1 electron configuration of Nb^{4+}. The replacement of calcium by magnesium does not introduce any transitions in the visible part of the spectrum and $MgZrF_6$ has a modest CTE at 300 K (α_V ~ -8 x10^{-6} K^{-1}), which crosses through zero at ~500 K. This suggests possible application in athermal multispectral optics for $MgZrF_6$ or appropriately substituted variants.

ASSOCIATED CONTENT

Supporting Information. Details of the diffraction data acquisition, high temperature diffraction data, example Rietveld fits, lattice constants versus temperature and pres-

sure. This material is available free of charge via the Internet at http://pubs.acs.org.

AUTHOR INFORMATION

Corresponding Author

* angus.wilkinson@chemistry.gatech.edu

Present Addresses

†Department of Chemistry, Northwestern University, 2145 Sheridan Road, Evanston, IL60208

Funding Sources

The work at Georgia Tech was partially supported under NSF DMR-1607316. A portion of this research used resources of the Advanced Photon Source, a U.S. Department of Energy (DOE) Office of Science User Facility operated for the DOE Office of Science by Argonne National Laboratory under Contract No. DE-AC02-06CH11357 and resources at the Spallation Neutron Source, a DOE Office of Science User Facility operated by the Oak Ridge National Laboratory.

ACKNOWLEDGEMENT

We are grateful for experimental assistance from the beam line staff of POWGEN at the SNS, and beam lines 11-IDB and 17-BM at the APS. We are grateful to Dr. Abbie Mclaughlin for her comments regarding strains at domain boundaries.

REFERENCES

1. Romao, C. P.; Miller, K. J.; Whitman, C. A.; White, M. A.; Marinkovic, B. A., Negative Thermal Expansion (Thermomiotic) Materials. In *Comprehensive Inorganic Chemistry II*, Reedijk, J.; Poeppelmeier, K. R., Eds. Elsevier: Oxford, 2013; Vol. 4, pp 128-151.
2. Lind, C., Two Decades of Negative Thermal Expansion Research: Where Do We Stand? *Materials* **2012,** *5* (6), 1125-1154.
3. Chen, J.; Hu, L.; Deng, J.; Xing, X., Negative thermal expansion in functional materials: controllable thermal expansion by chemical modifications. *Chem. Soc. Rev.* **2015,** *44* (11), 3522-3567.
4. Miller, W.; Smith, C. W.; Mackenzie, D. S.; Evans, K. E., Negative thermal expansion: a review. *J. Mater. Sci.* **2009,** *44* (20), 5441-5451.
5. Romao, C. P.; White, M. A., Negative stiffness in ZrW_2O_8 inclusions as a result of thermal stress. *Appl. Phys. Lett.* **2016,** *109* (3), 031902.
6. Lind, C.; Coleman, M. R.; Kozy, L. C.; Sharma, G. R., Zirconium tungstate/polymer nanocomposites: Challenges and opportunities. *Phys. Status Solidi B-Basic Solid State Phys.* **2011,** *248* (1), 123-129.
7. Holzer, H.; Dunand, D. C., Phase transformation and thermal expansion of Cu/ZrW_2O_8 metal matrix composites. *J. Mater. Res.* **1999,** *14*, 780-789.
8. Romao, C. P.; Marinkovic, B. A.; Werner-Zwanziger, U.; White, M. A., Thermal Expansion Reduction in Alumina-Toughened Zirconia by Incorporation of Zirconium Tungstate and Aluminum Tungstate. *J. Am. Ceram. Soc.* **2015,** *98* (9), 2858-2865.
9. Takenaka, K., Negative thermal expansion materials: technological key for control of thermal expansion. *Sci. Technol. Adv. Mater.* **2012,** *13* (1), 013001.
10. Della Gaspera, E.; Tucker, R.; Star, K.; Lan, E. H.; Ju, Y. S.; Dunn, B., Copper-Based Conductive Composites with Tailored Thermal Expansion. *ACS Appl. Mater. Interfaces* **2013,** *5* (21), 10966-10974.
11. Balch, D. K.; Dunand, D. C., Copper-Zirconium Tungstate Composites Exhibiting Low and Negative Thermal Expansion Influenced by Reinforcement Phase Transformations. *Metall. Mater. Trans. A* **2004,** *35A*, 1159-1165.
12. Morelock, C. R.; Suchomel, M. R.; Wilkinson, A. P., A cautionary tale on the use of GE-7031 varnish: Low temperature thermal expansion studies of ScF_3. *J. Appl. Crystallogr.* **2013,** *46*, 823-825.
13. Dove, M. T.; Fang, H., Negative thermal expansion and associated anomalous physical properties: review of the lattice dynamics theoretical foundation. *Rep. Prog. Phys.* **2016,** *79* (6), 066503.
14. Perottoni, C. A.; de Jornada, J. A. H., Pressure-Induced Amorphization and Negative Thermal Expansion in ZrW_2O_8. *Science* **1998,** *280*, 886-889.
15. Maczka, M.; Souza Filho, A. G.; Paraguassu, W.; Freire, P. T. C.; Mendes Filho, J.; Hanuza, J., Pressure-induced structural phase transitions and amorphization in selected molybdates and tungstates. *Prog. Mater. Sci.* **2012,** *57* (7), 1335-1381.
16. Varga, T.; Wilkinson, A. P.; Lind, C.; Bassett, W. A.; Zha, C.-S., In-situ high pressure synchrotron x-ray diffraction study of $Sc_2W_3O_{12}$ at up to 10 GPa. *Phys. Rev. B* **2005,** *71*, 214106 (1-8).
17. Varga, T.; Wilkinson, A. P.; Jupe, A. C.; Lind, C.; Bassett, W. A.; Zha, C.-S., Pressure-induced amorphization of cubic ZrW_2O_8 studied in-situ and ex-situ by synchrotron x-ray absorption spectroscopy and diffraction. *Phys. Rev. B* **2005,** *72*, 024117.
18. Hancock, J. C.; Chapman, K. W.; Halder, G. J.; Morelock, C. R.; Kaplan, B. S.; Gallington, L. C.; Bongiorno, A.; Han, C.; Zhou, S.; Wilkinson, A. P., Large negative thermal expansion and anomalous behavior on compression in cubic ReO_3-type $A^{II}B^{IV}F_6$: $CaZrF_6$ and $CaHfF_6$ *Chem. Mater.* **2015,** *27*, 3912-3918.
19. Zhao, Y.-Y.; Hu, F.-X.; Bao, L.-F.; Wang, J.; Wu, H.; Huang, Q.-Z.; Wu, R.-R.; Liu, Y.; Shen, F.-R.; Kuang, H.; Zhang, M.; Zuo, W.-L.; Zheng, X.-Q.; Sun, J.-R.; Shen, B.-G., Giant Negative Thermal Expansion in Bonded MnCoGe-Based Compounds with Ni2In-Type Hexagonal Structure. *J. Am. Chem. Soc.* **2015,** *137* (5), 1746-1749.
20. Azuma, M.; Chen, W. T.; Seki, H.; Czapski, M.; Olga, S.; Oka, K.; Mizumaki, M.; Watanuki, T.; Ishimatsu, N.; Kawamura, N.; Ishiwata, S.; Tucker, M. G.; Shimakawa, Y.; Attfield, J. P., Colossal negative thermal expansion in $BiNiO_3$ induced by intermetallic charge transfer. *Nat. Commun.* **2011,** *2*, 347.
21. Chen, J.; Nittala, K.; Forrester, J. S.; Jones, J. L.; Deng, J. X.; Yu, R. B.; Xing, X. R., The Role of Spontaneous Polarization in the Negative Thermal Expansion of Tetragonal $PbTiO_3$-Based Compounds. *J. Am. Chem. Soc.* **2011,** *133* (29), 11114-11117.
22. Rong, Y. C.; Li, M. L.; Chen, J.; Zhou, M.; Lin, K.; Hu, L.; Yuan, W. X.; Duan, W. H.; Deng, J. X.; Xing, X. R., Large negative thermal expansion in non-perovskite lead-free ferroelectric $Sn_2P_2S_6$. *Phys. Chem. Chem. Phys.* **2016,** *18* (8), 6247-6251.
23. Guo, X. G.; Lin, J. C.; Tong, P.; Wang, M.; Wu, Y.; Yang, C.; Song, B.; Lin, S.; Song, W. H.; Sun, Y. P., Magnetically driven negative thermal expansion in antiperovskite $Ga_{1-x}Mn_xN_{0.8}Mn_3$ ($0.1 \leq x \leq 0.3$). *Appl. Phys. Lett.* **2015,** *107* (20), 202406.
24. Yoon, D.; Son, Y. W.; Cheong, H., Negative Thermal Expansion Coefficient of Graphene Measured by Raman Spectroscopy. *Nano Lett.* **2011,** *11* (8), 3227-3231.
25. Morelock, C. R.; Gallington, L. C.; Wilkinson, A. P., Solid solubility, phase transitions, thermal expansion, and compressibility in $Sc_{1-x}Al_xF_3$. *J. Solid State Chem.* **2015,** *222*, 96-102.

26. Morelock, C. R.; Gallington, L. C.; Wilkinson, A. P., Evolution of negative thermal expansion and phase transitions in $Sc_{1-x}Ti_xF_3$. *Chem. Mater.* **2014,** *26* (5), 1936-1940.

27. Morelock, C. R.; Greve, B. K.; Gallington, L. C.; Chapman, K. W.; Wilkinson, A. P., Negative Thermal Expansion and Compressibility of $Sc_{1-x}Y_xF_3$ (x < 0.25). *J. Appl. Phys.* **2013,** *114*, 213501.

28. Greve, B. K.; Martin, K. L.; Lee, P. L.; Chupas, P. J.; Chapman, K. W.; Wilkinson, A. P., Pronounced Negative Thermal Expansion from a Simple Structure: Cubic ScF_3. *J. Am. Chem. Soc.* **2010,** *132* (44), 15496-15498.

29. Lazar, P.; Bučko, T.; Hafner, J., Negative thermal expansion of ScF_3: Insights from density-functional molecular dynamics in the isothermal-isobaric ensemble. *Phys. Rev. B* **2015,** *92* (22), 224302.

30. Hu, L.; Chen, J.; Fan, L.; Ren, Y.; Huang, Q.; Sanson, A.; Jiang, Z.; Zhou, M.; Rong, Y.; Wang, Y.; Deng, J.; Xing, X., High-Curie-Temperature Ferromagnetism in $(Sc,Fe)F_3$ Fluorides and its Dependence on Chemical Valence. *Adv. Mater.* **2015,** *27* (31), 4592-4596.

31. Li, C. W.; Tang, X.; Muñoz, J. A.; Keith, J. B.; Tracy, S. J.; Abernathy, D. L.; Fultz, B., Structural Relationship between Negative Thermal Expansion and Quartic Anharmonicity of Cubic ScF_3. *Phys. Rev. Lett.* **2011,** *107* (19), 195504.

32. Handunkanda, S. U.; Curry, E. B.; Voronov, V.; Said, A. H.; Guzmán-Verri, G. G.; Brierley, R. T.; Littlewood, P. B.; Hancock, J. N., Large isotropic negative thermal expansion above a structural quantum phase transition. *Phys. Rev. B* **2015,** *92* (13), 134101.

33. Hu, L.; Chen, J.; Xu, J.; Wang, N.; Han, F.; Ren, Y.; Pan, Z.; Rong, Y.; Huang, R.; Deng, J.; Li, L.; Xing, X., Atomic Linkage Flexibility Tuned Isotropic Negative, Zero, and Positive Thermal Expansion in $MZrF_6$ (M = Ca, Mn, Fe, Co, Ni, and Zn). *J. Am. Chem. Soc.* **2016,** *138* (44), 14530-14533.

34. Hu, L.; Chen, J.; Fan, L.; Ren, Y.; Rong, Y.; Pan, Z.; Deng, J.; Yu, R.; Xing, X., Zero Thermal Expansion and Ferromagnetism in Cubic $Sc_{1-x}M_xF_3$ (M = Ga, Fe) over a Wide Temperature Range. *J. Am. Chem. Soc.* **2014,** *136* (39), 13566-13569.

35. Yang, C.; Tong, P.; Lin, J. C.; Guo, X. G.; Zhang, K.; Wang, M.; Wu, Y.; Lin, S.; Huang, P. C.; Xu, W.; Song, W. H.; Sun, Y. P., Size effects on negative thermal expansion in cubic ScF3. *Appl. Phys. Lett.* **2016,** *109* (2), 023110.

36. Reinen, D.; Steffens, F., Structure and Bonding in Transition-Metal Fluorides $M^{II}Me^{IV}F_6$ .A. Phase-Transitions. *Z. Anorg. Allg. Chem.* **1978,** *441* (4), 63-82.

37. Babel, D.; Tressaud, A., Crystal Chemistry of Fluorides. In *Inorganic Solid Fluorides*, Hagenmuller, P., Ed. Academic Press, Inc.: Orlando, 1985; pp 78-203.

38. Rodriguez, V.; Couzi, M.; Tressaud, A.; Grannec, J.; Chaminade, J. P.; Soubeyroux, J. L., Structural Phase-Transition in the Ordered Fluorides $M^{II}ZrF_6$ (M^{II} = Co, Zn).1. Structural Study. *J. Phys. Condens. Matter* **1990,** *2* (36), 7373-7386.

39. Chassaing, J.; Bizot, D., Synthesis, Spectroscopic and Magnetic Study of NbF_4. *J. Fluorine Chem.* **1980,** *16* (5), 451-459.

40. Gortsema, F. P.; Didchenko, R., Preparation and Properties of Niobium Tetrafluoride and Oxyfluorides. *Inorg. Chem.* **1965,** *4* (2), 182-186.

41. Goubard, F.; Llorente, S.; Gaubicher, J.; Bizot, D.; Chassaing, J., Powder diffraction data for fluorocomplexes of niobium IV: $MNbF_6$ (M=Ca, Mg, Cd, Zn). *Powder Diffr.* **1998,** *13* (3), 163-165.

42. Wang, J.; Toby, B. H.; Lee, P. L.; Ribaud, L.; Antao, S. M.; Kurtz, C.; Ramanathan, M.; Von Dreele, R. B.; Beno, M. A., A dedicated powder diffraction beamline at the Advanced Photon Source: Commissioning and early operational results. *Rev. Sci. Instrum.* **2008,** *79* (8), 085105.

43. Lee, P. L.; Shu, D.; Ramanathan, M.; Preissner, C.; Wang, J.; Beno, M. A.; Von Dreele, R. B.; Ribaud, L.; Kurtz, C.; Antao, S. M.; Jiao, X.; Toby, B. H., A twelve-analyzer detector system for high-resolution powder diffraction. *J. Synchrotron Rad.* **2008,** *15*, 427-432.

44. Birch, F., Equation of state and thermodynamic parameters of sodium chloride to 300 kbar in the high-temperature domain. *J. Geophys. Res. B* **1986,** *91* (B5), 4949-4954.

45. Angel, R. J., The high-pressure, high tempertaure equation of state of calcium fluoride, CaF_2. *J. Phys. Condens. Matter* **1993,** *5* (11), L141-L144.

46. Wilkinson, A. P.; Morelock, C. R.; Greve, B. K.; Jupe, A. C.; Chapman, K. W.; Chupas, P. J.; Kurtz, C., Reducing the background from pressure vessels using a BRIM. *J. Appl. Crystallogr.* **2011,** *44*, 1047-1053.

47. Larson, A. C.; Von Dreele, R. B., *GSAS - General Structure Analysis System*. Report LA-UR-86-748: Los Alamos Laboratory, 1987.

48. Toby, B. H., EXPGUI, a graphical user interface for GSAS. *J. Appl. Crystallogr.* **2001,** *34*, 210-213.

49. Niedervahrenholz, H. G.; Schafer, H., Oxidefluorides of niobium and tantalum. *Z. Anorg. Allg. Chem.* **1987,** *544* (1), 122-126.

50. Boysen, H., Ferroelastic phase transitions and domain structures in powders. *Z. Kristallogr.* **2005,** *220* (8), 726-734.

51. Poulain, M.; Lucas, J., The system MF_2-ZrF_4 (M=Mg,Mn,Fe,Co,Ni,Zn). The fluorozirconates of the cubic rare earths. *Rev. Chem. Miner.* **1975,** *12* (1), 9-16.

52. Gonzalez-Platas, J.; Alvaro, M.; Nestola, F.; Angel, R., EosFit7-GUI: a new graphical user interface for equation of state calculations, analyses and teaching. *J. Appl. Crystallogr.* **2016,** *49* (4), 1377-1382.

53. Angel, R. J.; Gonzalez-Platas, J.; Alvaro, M., EosFit7c and a Fortran module (library) for equation of state calculations. *Z. Kristallogr.* **2014,** *229* (5), 405-419.

54. Fang, H.; Phillips, A. E.; Dove, M. T.; Tucker, M. G.; Goodwin, A. L., Temperature-dependent pressure-induced softening in $Zn(CN)_2$. *Phys. Rev. B* **2013,** *88* (14), 144103.

55. Chapman, K. W.; Chupas, P. J., Pressure Enhancement of Negative Thermal Expansion Behavior and Induced Framework Softening in Zinc Cyanide. *J. Am. Chem. Soc.* **2007,** *129* (33), 10090-10091.

56. Fang, H.; Dove, M. T.; Phillips, A. E., Common origin of negative thermal expansion and other exotic properties in ceramic and hybrid materials. *Phys. Rev. B* **2014,** *89* (21), 214103.

57. Fang, H.; Dove, M. T., A phenomenological expression to describe the temperature dependence of pressure-induced softening in negative thermal expansion materials. *J. Phys. Condens. Matter* **2014,** *26* (11), 115402.

58. Fang, H.; Dove, M. T., Pressure-induced softening as a common feature of framework structures with negative thermal expansion. *Phys. Rev. B* **2013,** *87* (21), 214109.

Insert Table of Contents artwork here